Nano-electrochemistry & Nano-photochemistry
https://www.sciltp.com/journals/nenp

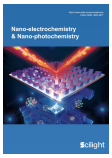

Article

Check for updates

Homogeneous Multicolor Perovskite Quantum Dots Enable Ratiometric Profiling of Pan-Deubiquitinating Activity in Perioperative Neurocognitive Disorders Blood Samples

Rongjin Shi [1,2], Siyi Han [1] and Enduo Feng [1,*]

[1] School of Chemical Science and Engineering, Tongji University, Shanghai 200092, China
[2] Shanghai Key Laboratory of Anesthesiology and Brain Functional Modulation, Clinical Research Center for Anesthesiology and Perioperative Medicine, Translational Research Institute of Brain and Brain-Like Intelligence, Shanghai Fourth People's Hospital, School of Medicine, Tongji University, Shanghai 200434, China
* Correspondence: edfeng@tongji.edu.cn

How To Cite: Shi, R.; Han, S.; Feng, E. Homogeneous Multicolor Perovskite Quantum Dots Enable Ratiometric Profiling of Pan-Deubiquitinating Activity in Perioperative Neurocognitive Disorders Blood Samples. *Nano-electrochemistry & Nano-photochemistry* **2026**, *2*(2), 12. https://doi.org/10.53941/nenp.2026.100012

Received: 14 February 2026
Revised: 27 April 2026
Accepted: 14 May 2026
Published: 8 June 2026

Abstract: Perioperative neurocognitive disorders (PND) represent a prevalent and clinically challenging complication following surgery and anesthesia. However, reliable peripheral biomarkers capable of reflecting molecular dysfunction in complex biofluids remain scarce. Dysregulation of the ubiquitin-proteasome system has been increasingly implicated in perioperative neuroinflammation and synaptic dysfunction. Herein, we develop a homogeneous dual-emission ratiometric fluorescent platform based on compositionally correlated perovskite quantum dots (PQDs) for robust profiling of Pan-deubiquitinating enzyme (pan-DUB) activity in perioperative blood samples. Specifically, green-emissive $CsPbBr_3$ PQDs were engineered as the enzyme-responsive channel, while orange-emissive $CsPbBr_{1.5}I_{1.5}$ PQDs served as an internal reference. Notably, both $CsPbBr_3$ and $CsPbBr_{1.5}I_{1.5}$ PQDs shared a unified lattice framework and surface chemistry through conformal SiO_2 encapsulation, enabling intrinsically matched photophysical responses to different environmental perturbations. By coupling a ubiquitin-derived peptide, pan-DUB-mediated cleavage induced a ratiometric fluorescence increase without perturbing the reference signal, achieving high sensitivity within the range of 0.01–0.5 IU/mL. The limit of detection was calculated to be 0.004 IU/mL. Finally, as-prepared PQD-based sensing platform with high sensitivity and excellent anti-interference was employed to determine the pan-DUB activity in mouse serum of PND. A significant elevation of serum pan-DUB activity following surgery was clearly observed, which strongly correlated with deficits in spatial working memory. Moreover, receiver operating characteristic analysis demonstrated the high discriminative power for distinguishing PND from sham-operated animals (AUC = 1.00). This work established a homogeneous multicolor ratiometric sensing strategy that enabled accurate functional profiling of pan-DUB activity in complex biofluids, offering mechanistic insight and a promising peripheral biomarker approach for perioperative neurocognitive disorders.

Keywords: perioperative neurocognitive disorders; perovskite quantum dots; pan-deubiquitinating enzyme activity; ratiometric fluorescence quantification

1. Introduction

Perioperative neurocognitive disorders (PND) represent a spectrum of cognitive impairments that occur in the perioperative period and are particularly prevalent among elderly patients undergoing major surgery under general anesthesia [1,2]. PND is associated with prolonged hospitalization, increased morbidity, and long-term decline in quality of life [3]. Despite its clinical significance, the molecular mechanisms underlying PND remain incompletely understood, and reliable peripheral biomarkers capable of reflecting perioperative neurobiological stress responses are still lacking [4,5]. Accumulating evidence indicates that perioperative insults, including systemic inflammation, metabolic stress, and anesthetic exposure, profoundly perturb protein homeostasis in both the central nervous system and peripheral immune compartments [6]. The ubiquitin-proteasome system (UPS) plays a central role in maintaining proteostasis by dynamically regulating protein ubiquitination (UB) and deubiquitination (DUB). Dysregulation of ubiquitin-dependent protein turnover has been implicated in neuroinflammation, synaptic dysfunction, and impaired stress adaptation, all of which contribute to the pathogenesis of PND [7–9]. Pan-deubiquitinating enzyme (pan-DUB) activity has emerged as a functionally integrative phenotype that reflects the collective status of deubiquitination pathways, representing a promising biomarker for clinical diagnosis and risk prediction of PND.

Several analytical strategies have been developed for profiling pan-deubiquitinating (pan-DUB) activity. Fluorogenic ubiquitin substrates such as Ub-Rhodamine110 and Ub-AMC are standard tools with high sensitivity in purified enzyme systems and cell lysates [10]. Electrochemical sensors provide rapid and miniaturized detection of DUB activity [11], while Western blotting (WB) enables semi-quantitative analysis with high specificity [12]. However, the application of intensity-based DUB assays to perioperative blood-derived samples presents fundamental challenges. Perioperative serum or cellular lysates exhibit substantial heterogeneity in protein content, endogenous fluorophores, hemoglobin-derived absorption, and light scattering, which can distort fluorescence amplitude and compromise quantitative comparability across patients and time points [13,14]. Ratiometric fluorescence sensing addresses this challenge. It uses a single excitation environment and effectively suppresses optical interference, enabling robust detection in heterogeneous biofluids [15]. However, conventional multicolor organic fluorophores with distinct emission wavelengths inevitably possess different chemical structures, surface functionalities, and excited-state properties, rendering their photophysical responses unequally sensitive to environmental factors such as pH, ionic strength, redox species, protein adsorption, and endogenous interferents [16]. As a result, matrix interference often influences each channel differently, reducing the accuracy of ratiometric signals [17].

Advanced nanomaterials and biosensing technologies have been widely explored in biomedical applications [18–24]. Notably, the emission color of metal halide perovskite quantum dots (PQDs) is governed primarily by composition rather than by distinct molecular chromophores, allowing spectrally separated PQDs to be engineered with nearly identical surface chemistry, encapsulation, and interfacial environments [25,26]. Such structural homogeneity ensures that different-color PQDs show highly consistent responses to nonspecific environmental interference, while maintaining excellent optical distinguishability. These features enable multicolor PQDs to serve as chemically matched ratiometric signal pairs with minimized channel-dependent interference, making them ideal for building intrinsically calibrated ratiometric probes for functional enzyme detection in complex biological samples [27–29].

In this work, we report a multicolor perovskite quantum dot (PQD)-based ratiometric probe for quantitative profiling of pan-deubiquitinating (pan-DUB) activity in perioperative neurocognitive disorder (PND) blood samples. Green-emissive PQDs $CsPbBr_3$ with a maximum emission at 520 nm was employed as the DUB-responsive channel, while a red-emissive PQD $CsPbBr_{1.5}/I_{1.5}$ emitting at 588 nm was used as an internal reference. Both PQD populations were first encapsulated using a thin SiO_2 shell to ensure an excellent water stability and chemically matched responses in complex blood matrices. Then, Pan-DUB activity was transduced by coupling a ubiquitin-derived cleavage motif to a proximal fluorescence-quenching element on the green-emissive PQD. Enzymatic deubiquitination induced a turn-on recovery of green emission, while the reference channel remained optically invariant. Under optimized conditions, the ratiometric signal $R = I_{520}/I_{588}$ exhibited a linear response to pan-DUB activity over a range of 0.01–0.5 IU/mL, achieving a limit of detection of 0.004 IU/mL. Notably, the ratiometric PQD platform preserved excellent signal linearity and sensitivity in protein-rich and optically heterogeneous matrices with a spearman $r = 0.99$, inferring the great anti-interference ability of the dual-emission PQD sensing platform, which was suitable for precise quantification of enzymatic pan-DUB activity in patients' blood sample. Moreover, compared with established fluorogenic substrates, including Ub-Rhodamine110 and Ub-AMC, the PQD-based ratiometric probe displayed comparable sensitivity in buffered systems, but demonstrated a reduced inter-sample coefficient of variation of 94% in perioperative blood matrices under identical assay

conditions, highlighting the suitability of multicolor PQD-enabled ratiometric readout for robust functional profiling of ubiquitin system activity in complex clinical specimens. Finally, dual-emission PQD-based assay was subjected to investigate the pan-DUB level of blood samples collected from a perioperative neurocognitive disorder (PND) mouse model. Compared with the control sham group, pan-DUB activity in PND mice was found to increase significantly, indicating a global enhancement of deubiquitination dynamics in the perioperative cognitive dysfunction state. Collectively, this work established a multicolor perovskite quantum dot-enabled ratiometric strategy for robust profiling of pan-deubiquitinating activity in perioperative blood samples. By transforming enzyme activity into an internally calibrated ratiometric signal, the proposed probe enabled reliable functional differentiation between PND and control states and provided a generalizable platform for interrogating ubiquitin system dynamics in heterogeneous biological matrices.

2. Experimental Section

2.1. Materials

Cesium carbonate (Cs_2CO_3), lead bromide ($PbBr_2$), lead iodide (PbI_2), 1-octadecene (ODE, 90%), oleic acid (OA, 90%), oleylamine (OAm, 70%), tetraethyl orthosilicate (TEOS), (3-aminopropyl)triethoxysilane (APTES), EDC·HCl, N-hydroxysuccinimide (NHS), Tris, MES, DTT, NaCl, $MgCl_2$, ethanol, hexane, cyclohexane, and Igepal CO-520 were purchased from Sigma-Aldrich unless otherwise specified. Ubiquitin-derived peptide bearing terminal carboxyl group and DCQ quencher was custom synthesized (>95% purity). Recombinant pan-deubiquitinase (pan-DUB) enzyme mixture and Ub-AMC substrate were obtained commercially. Fetal bovine serum (FBS) was purchased from Gibco. Ultrapure water (18.2 MΩ·cm) was used throughout. The pan-DUB substrate was constructed as Ub(1-76)-GGG-DCQ, in which full-length human ubiquitin preserved its native C-terminal Gly-Gly recognition motif, followed by a tri-glycine linker and a terminal dark quencher (DCQ) conjugated via amide coupling at the ubiquitin C-terminus.

2.2. Synthesis of Cs-oleate Precursor

Cs_2CO_3 (0.407 g, 1.25 mmol), ODE (20 mL), and OA (1.25 mL) were loaded into a 50 mL three-neck flask. The mixture was degassed under vacuum at 120 °C for 30 min and then heated to 150 °C under nitrogen until complete dissolution, yielding Cs-oleate precursor, which was maintained at 100–120 °C prior to injection.

2.3. Synthesis of $CsPbBr_3$ Perovskite Quantum Dots

$PbBr_2$ (0.138 g, 0.376 mmol) and ODE (10 mL) were added to a three-neck flask and degassed at 120 °C for 30 min. After nitrogen purging, OA (1.0 mL) and OAm (1.0 mL) were injected and stirred until a clear solution formed. The temperature was raised to 170 °C, followed by rapid injection of Cs-oleate (0.8 mL). After 5–10 s of growth, the reaction was quenched by immersion in an ice-water bath. The crude product was centrifuged after adding methyl acetate as antisolvent (1:2 *v*/*v*). The precipitate was redispersed in hexane and further purified once using mild antisolvent treatment. Final $CsPbBr_3$ PQDs were stored in hexane at 4 °C in the dark.

2.4. Synthesis of $CsPbBr_{1.5}I_{1.5}$ Perovskite Quantum Dots

Mixed-halide PQDs were prepared following the same protocol, except $PbBr_2$ and PbI_2 were introduced at equimolar ratio while keeping total Pb^{2+} constant. Injection temperature was maintained at 160–170 °C, and growth time was limited to 5–10 s to suppress halide segregation. Purification was performed under milder conditions to preserve surface ligands.

2.5. SiO_2 Encapsulation of PQDs

PQDs were coated with an ultrathin SiO_2 shell (~2 nm) using a reverse microemulsion approach. Purified PQDs (OD ≈ 1 at first excitonic peak) were dispersed in cyclohexane (10 mL) containing Igepal CO-520 (0.8 mL). NH_4OH (28 wt%, 100 μL) was added to form nanoscale aqueous domains, followed by dropwise addition of TEOS (25 μL, pre-diluted). The reaction proceeded at room temperature for 6 h. Ethanol (15 mL) was added to break the emulsion, and particles were collected by centrifugation (8000 rpm, 10 min), washed twice with ethanol, and redispersed in ethanol or water.

2.6. Surface Amination and Peptide-DCQ Conjugation

$CsPbBr_3@SiO_2$ nanoparticles were dispersed in ethanol (1 mg mL^{-1}) and reacted with APTES (2% *v*/*v*) for 3 h to introduce surface amine groups. Ub-peptide-DCQ bearing terminal -COOH was activated in MES buffer (50 mM, pH 5.5) with EDC (2 mM) and NHS (5 mM) for 15 min and subsequently added to $CsPbBr_3@SiO_2$-NH_2 in PBS (pH 7.4). The reaction proceeded overnight at room temperature, forming amide bonds. After purification by centrifugation and washing, $CsPbBr_3@SiO_2$-peptide-DCQ was obtained as the green-responsive channel. $CsPbBr_{1.5}I_{1.5}@SiO_2$ nanoparticles served as the orange internal reference without further modification.

2.7. Assembly of Dual-Emission Ratiometric Probe

Green $CsPbBr_3@SiO_2$-peptide-DCQ and orange $CsPbBr_{1.5}I_{1.5}@SiO_2$ were mixed at final concentrations of 1.8 nM each, normalized by emission intensity to ensure comparable baseline signals. The probe was equilibrated in PBS (pH 7.4) for 10 min prior to use. Ratiometric signal was defined as: $R = I_{520}/I_{588}$.

2.8. pan-DUB Activity Assay

All enzymatic reactions were performed in DUB buffer (50 mM Tris-HCl, pH 7.5, 150 mM NaCl, 5 mM DTT, 1 mM $MgCl_2$). Different pan-DUB activities (0–2.0 IU mL^{-1}) were incubated with the probe (200 μL total volume) at 37 °C for 30 min. Fluorescence spectra were recorded under 405 nm excitation. LOD was calculated using 3σ/k.

2.9. Kinetic Measurements

Real-time fluorescence ratios were recorded over 60 min at 0.1, 0.5, and 1.0 IU mL^{-1} pan-DUB.

2.10. Selectivity, Competition, and Environmental Robustness

Interferents including ions, proteins, enzymes, metabolites, and nucleases were evaluated under identical conditions. Competition assays were conducted by co-incubating pan-DUB with interferents. Environmental robustness was examined in PBS, 10% and 50% FBS, high-salt buffer (300 mM NaCl), pH 5.5, pH 9.0, hemolyzed (2–5 mg mL^{-1} hemoglobin), and lipemic (200–500 mg dL^{-1} triglycerides) matrices at low, medium, and high enzyme activities.

2.11. Stability Tests

Photostability was assessed over 50 excitation cycles. Storage stability was evaluated after aqueous storage at 4 °C for 30 days. R/R_0 was calculated (n = 3).

2.12. Animal Model and Behavioral Testing

Male C57BL/6J mice were subjected to laparotomy under isoflurane anesthesia to establish PND model. Sham mice received anesthesia only. Spatial working memory was evaluated using Y-maze spontaneous alternation. All experiments were performed according to the Chinese Council on Animal Care Guidelines and approved by the Tongji University Animal Ethics Committee (TJBH00921101).

2.13. Serum pan-DUB Measurement

Blood was collected, centrifuged to obtain serum, and incubated with probe. Equivalent pan-DUB activity was calculated from calibration curves.

2.14. Statistical Analysis

Data are presented as mean ± S.D. Pearson correlation and ROC analysis were performed using GraphPad Prism.

2.15. Calculation Method

The limit of detection (LOD) was calculated according to the IUPAC standard formula:

$$LOD = \frac{3 \times SD_0}{k}$$

SD_0 is the standard deviation of 10 replicate measurements of the blank solution, and k is the slope of the calibration curve between the ratiometric fluorescence signal and pan-DUB activity.

3. Results and Discussion

3.1. Characterization of $CsPbBr_3$ and $CsPbBr_{1.5}I_{1.5}$ Nanocrystals

Colloidal $CsPbBr_3$ and $CsPbBr_{1.5}I_{1.5}$ perovskite nanocrystals (NCs) were synthesized through a reported protocol previously and subsequently encapsulated with an amorphous SiO_2 shell to enhance their environmental robustness in aqueous conditions [30,31]. As shown in Figure S1, the as-prepared NCs exhibit a uniform cubic-like morphology with average edge lengths of 25 ± 3 nm. After SiO_2 encapsulation, a conformal amorphous shell with a thickness of ~2–3 nm is observed, forming a continuous inorganic barrier without compromising the internal lattice integrity. Moreover, high-resolution transmission electron microcopy (HR-TEM) revealed distinct lattice fringes of ~0.41 nm in Figure 1A, corresponding to the (002) planes of the perovskite crystal structure of $CsPbBr_3$, indicating high crystallinity and minimal internal defects. Comparably, $CsPbBr_{1.5}I_{1.5}$ NCs displayed a relative larger lattice fringe of ~0.43 nm (Figure 1B), which should be ascribed to the lattice expansion induced by partial substitution of Br^- by the larger I^- ions. X-ray diffraction (XRD) patterns of $CsPbBr_3$ and $CsPbBr_{1.5}I_{1.5}$ NCs (Figure 1C) showed distinctive XRD peaks corresponding to the cubic perovskite phase (PDF#054-0752). Compared with $CsPbBr_3$, XRD peaks of $CsPbBr_{1.5}I_{1.5}$ NCs exhibited a left-shift, further confirming the substitution of Br^- by the larger I^- ions. More importantly, both $CsPbBr_3$@SiO_2 and $CsPbBr_{1.5}I_{1.5}$@SiO_2 compositions retained the characteristic diffraction peaks of the cubic perovskite phase after encapsulation. No secondary phases or peak splitting are detected, suggesting that the SiO_2 shell neither interferes with the native crystallographic symmetry nor alters the halide distribution [32].

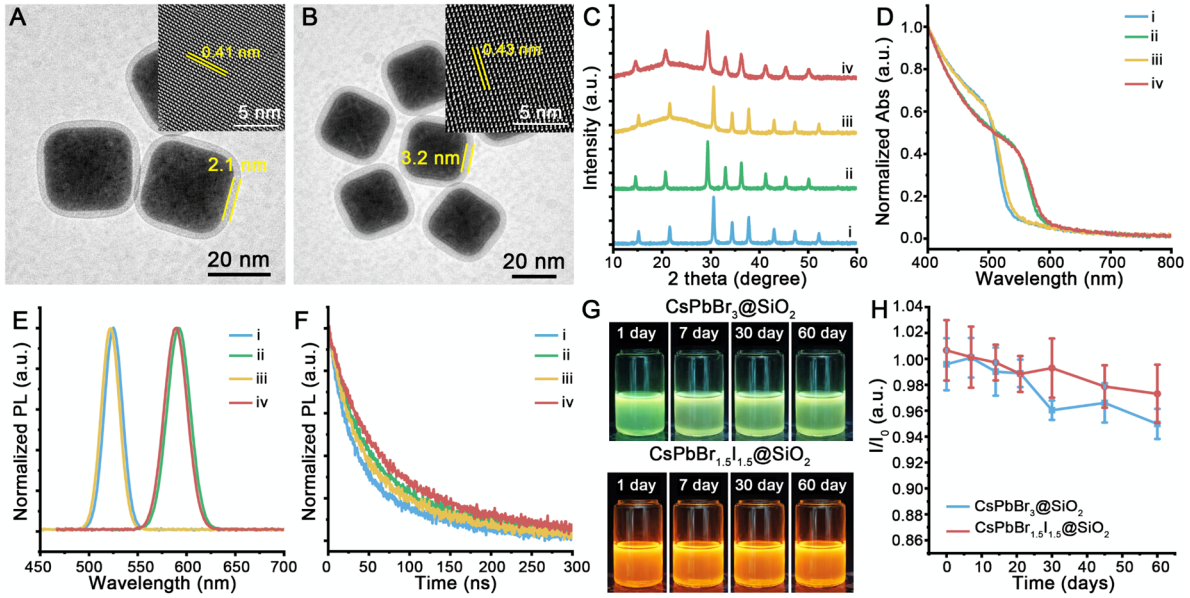

Figure 1. Characterization of $CsPbBr_3$ and $CsPbBr_{1.5}I_{1.5}$ with SiO_2 encapsulation. (**A**,**B**) TEM and inset: HR-TEM images of (**A**) $CsPbBr_3$ and (**B**) $CsPbBr_{1.5}I_{1.5}$. (**C**–**F**) (**C**) XRD patterns, (**D**) UV-vis absorption spectra, (**E**) Steady-state PL and (**F**) time-resolved PL measurements of (i) $CsPbBr_3$, (ii) $CsPbBr_{1.5}I_{1.5}$, (iii) $CsPbBr_3$@SiO_2 and (iv) $CsPbBr_{1.5}I_{1.5}$@SiO_2. (**G**) Photographs under UV illumination of $CsPbBr_3$@SiO_2 and $CsPbBr_{1.5}I_{1.5}$@SiO_2 storage for different times. (**H**) PL stability analysis (I/I_0) of $CsPbBr_3$@SiO_2 and $CsPbBr_{1.5}I_{1.5}$@SiO_2 storage for different times (n = 5). All samples were stored at 4 °C in aqueous suspension during the 60-day stability test.

Meanwhile, the UV-vis absorption spectra of $CsPbBr_3$ and $CsPbBr_{1.5}I_{1.5}$ NCs (Figure 1D) showed well-defined band-edge onsets. Specifically, $CsPbBr_3$ exhibited an absorption edge at 515 nm, while partial substitution of Br^- with the larger I^- anion induced a red-shift to ~560–570 nm, confirming effective bandgap narrowing due to lattice expansion and strengthened electronic coupling within the Pb-X framework. Importantly, no additional sub-bandgap absorption or tail states were introduced after SiO_2 encapsulation, indicating that the shell formation preserved the intrinsic electronic configuration without causing interfacial energy disorder. Furthermore, steady-state Photoluminescence (PL) spectra (Figure 1E) of $CsPbBr_3$ showed green emission centered at ~520 nm, whereas $CsPbBr_{1.5}I_{1.5}$ exhibited an orange emission peak at ~588 nm, which was highly consistent with iodide-

induced bandgap reduction. After SiO_2 encapsulation, both compositions retain nearly identical emission maxima with a slightly blue shift, suggesting that the shell effectively suppressed surface deformation of the water environment without altering internal emissive states. Time-resolved PL decay curves (Figure 1F) revealed clear differences in carrier recombination dynamics with biexponential decay behavior, including the fast surface-related recombination and slow radiative recombination processes. Uncoated $CsPbBr_3$ and $CsPbBr_{1.5}I_{1.5}$ NCs nanocrystals display faster decay with an average lifetime (τ) of 55 ns ($CsPbBr_3$) and 75 ns ($CsPbBr_{1.5}I_{1.5}$). In contrast, SiO_2-coated samples present extended lifetimes with $\tau = 66$ ns for $CsPbBr_3$ and $\tau = 90$ ns for $CsPbBr_{1.5}I_{1.5}$, which were consistent with inhibited non-radiative pathways and reduced defect-assisted exciton quenching. Also, the absolute photoluminescence quantum yield (PLQY) of the as-synthesized $CsPbBr_3$ was measured to be ~69.7%. After conformal SiO_2 encapsulation, the PLQY increased to ~77.2%, which can be attributed to effective surface passivation and suppression of non-radiative recombination pathways.

Finally, the most prominent improvement of the long-term aqueous stability of two NCs was well characterized in Figure 1G,H. Significantly, uncoated $CsPbBr_3$ and $CsPbBr_{1.5}I_{1.5}$ NCs underwent rapid fluorescence loss within several days, accompanied by visual turbidity, phase decomposition, and color variation (Figure S2). In stark contrast, due to the dense SiO_2 network as both a physical diffusion barrier against water ingress and an electrostatic confinement layer, SiO_2-coated NCs remained optically and morphologically stable for 60 days, maintaining >95% of their initial PL intensity ($n = 5$), confirming that encapsulation fundamentally altered the perovskite-water interfacial chemistry, and decoupling environmental stress from structural and electronic degradation.

3.2. Fabrication of Dual Emission Ratiometric pan-DUB Fluorescent Probe

To construct a robust ratiometric fluorescent probe for pan-DUB sensing, a stepwise surface engineering strategy was implemented to integrate APTES functionalization, and terminal DUB-peptide grafting on NCs@SiO_2 surface (Figure 2A), establishing a dual-emission system in which the $CsPbBr_3$ with green emission acted as the response channel and $CsPbBr_{1.5}I_{1.5}$ NCs with orange emission served as an internal reference for self-calibrated fluorescence output during biochemical interactions [33]. As illustrated in Figure 3A, the peptide-functionalized $CsPbBr_3$@SiO_2 nanocrystal exhibits suppressed green emission via proximity-induced non-radiative energy transfer from the perovskite donor to the (4-[(4-dimethylaminophenyl)azo]benzoic acid (DCQ) acceptor, whereas the $CsPbBr_{1.5}I_{1.5}$@SiO_2 reference nanocrystal maintains a stable orange signal. The progressive surface modification at each stage was confirmed by FTIR spectra (Figure 2B). Notably, the pristine SiO_2-coated particles displayed characteristic Si-O-Si stretching vibrations in the range of 950–1100 cm^{-1}, while APTES modification introduced pronounced N-H and C-H vibrations, indicating the successful introduction of amine-terminated organosilane ligands [34]. After peptide grafting, new amide-related bands emerged near ~1650 cm^{-1}, confirming the covalent coupling between the -COOH of the peptide and the -NH_2 of APTES interface [35]. Moreover, the stepwise surface modifications also measured by ζ-potential analysis, which revealed a transition from negative values of −19.68 mV for SiO_2-coated nanocrystals to strongly positive surface charge of +10.94 mV after APTES grafting, followed by partial charge neutralization after peptide conjugation (Figure 2C). Similarly, dynamic light scattering (DLS) results also demonstrated a controllable hydrodynamic size increase from ~23 nm to ~30 nm across the three modification stages (Figure 2D), indicating the successful and uniform construction of the interfacial organic layers.

In addition, the stepwise fabrication process was further characterized by fluorescent spectra (Figure 2E) with a dual-emission ratiometric framework. Significantly, the green emission at 520 nm (I_{green}) originating from $CsPbBr_3$ decreased progressively upon peptide functionalization due to fluorescence quenching, while the orange emission at 588 nm (I_{orange}) remained nearly constant across samples with only ±1% fluctuation, which allowed ratiometric quantification via the ratio $R = I_{green}/I_{orange}$, effectively eliminating interference from environmental fluctuations, probe concentration variance, and excitation power instability. To further evaluate long-term stability, illumination endurance and long-term storage stability were examined. As shown in Figure 2F, after 50 irradiation cycles, the dual-emission ratio maintained >95% ($\Delta R = (R - R_0)/R_0$) of its initial value with negligible drift, indicating excellent photostability. Likewise, storage tests over 30 days showed a gradual but well-controlled nonlinear attenuation trend, which is consistent with slow interfacial relaxation while still maintaining sufficient sensing fidelity (>95%) (Figure 2G). Collectively, these results confirmed that the silica-protected, APTES-bridged, peptide-functionalized perovskite nanocrystals achieve structural robustness, interfacial specificity, and optical self-calibration. More importantly, the ratiometric fluorescence response provided a reliable foundation for biomolecular recognition and quantitative pan-DUB activity analysis.

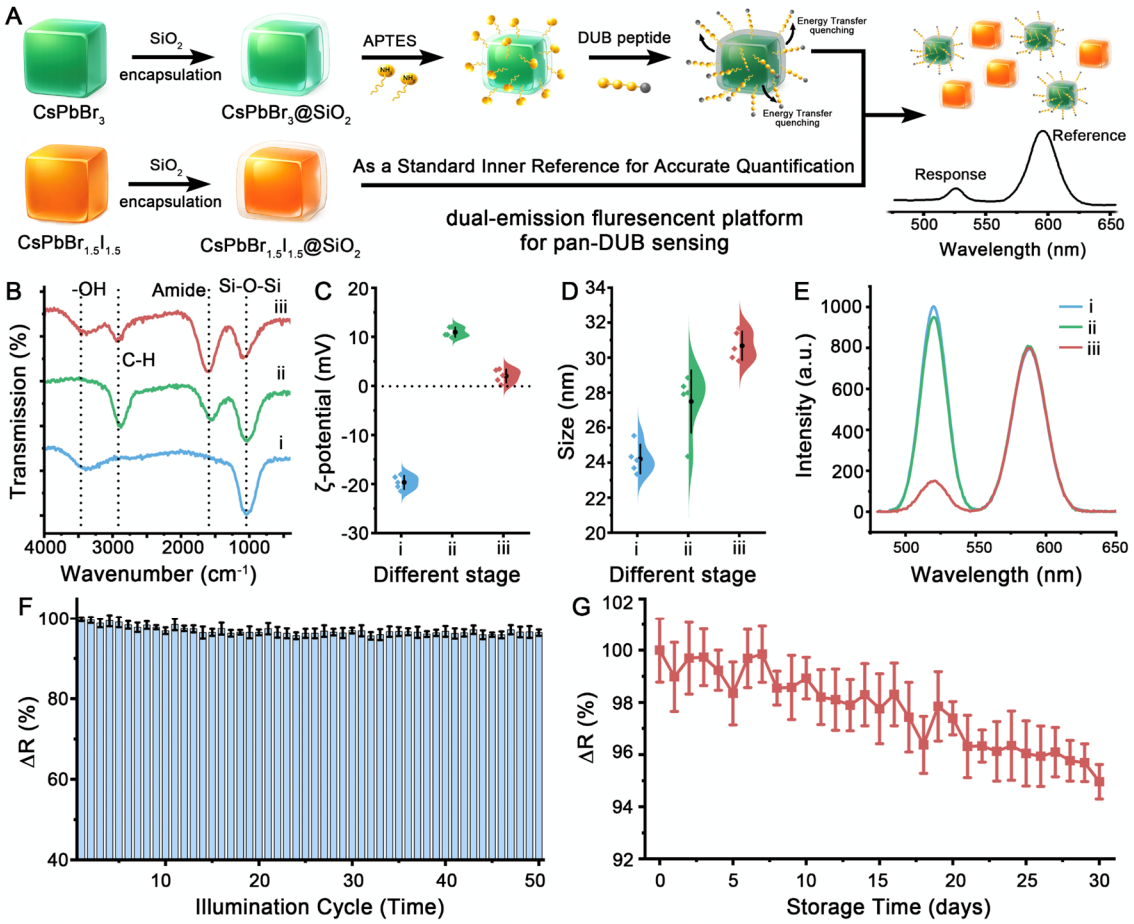

Figure 2. Construction and characterization of the dual-emission ratiometric probe. (**A**) Schematic illustration of the stepwise surface engineering strategy to form a dual-emission fluorescent system. (**B**–**D**) (**B**)FT-IR spectra, (**C**) ζ-potential and (**D**) hydrodynamic size variations of (i) $CsPbBr_3$@SiO_2, (ii) $CsPbBr_3$@SiO_2-APTES and (iii) $CsPbBr_3$@SiO_2-peptide. (**E**) Dual-emission PL spectra of (i) $CsPbBr_3$@SiO_2, (ii) $CsPbBr_3$@SiO_2-APTES and (iii) $CsPbBr_3$@SiO_2-peptide. (**F**) Photostability analysis of $\Delta R = (R - R_0)/R_0$ over 50 illumination cycles. (**G**) Storage stability of $\Delta R = (R - R_0)/R_0$ over 30 days.

3.3. Response Evaluation of Dual Emission Ratiometric pan-DUB Fluorescent Probe

The response behavior of the dual-emission probe was first examined to validate its applicability for pan-DUB activity determination. In the absence of pan-DUB, DCQ quenches the green emission of $CsPbBr_3$@SiO_2 via proximity-induced non-radiative energy transfer, while the orange reference signal remains unchanged. Significantly, peptide cleavage was induced by pan-DUB catalytic process, resulting in a disruption of the DCQ quenching pathway, which was led by the detachment of DCQ from the $CsPbBr_3$@SiO_2 surface. Then, a regeneration of the green emission channel was clearly observed, which yielded a measurable change in the fluorescence ratio $R = I_{green}/I_{orange}$ for ratiometric quantification of pan-DUB activity, significantly eliminating the environmental interferences and enabling robust and reliable quantification in complex blood matrix. As shown in Figure S3, before enzymatic reaction (quenched state), the probe showed a short average lifetime of 26 ns. Comparably, a significant average lifetime increase of 61 ns was observed after pan-DUB-mediated substrate cleavage, which was induced by the absence of energy transfer quenching effects from $CsPbBr_3$@SiO_2 to DCQ. Meanwhile, different from $CsPbBr_3$@SiO_2, $CsPbBr_{1.5}I_{1.5}$@SiO_2 exhibited a longer but stable average lifetime of 89 ns, suggesting a stable microenvironment of $CsPbBr_{1.5}I_{1.5}$@SiO_2 during the pan-DUB-mediated substrate cleavage. Quantitatively, fluorescence spectra (Figure 3B) presented a clear activity-dependent enhancement in the green emission channel across 0.01–2.0 IU/mL, while the reference peak remains essentially unchanged, confirming robust internal self-calibration. As shown in Figure 3C, the R value increased with the pan-DUB activity progressively within the range of 0–2.0 IU/mL. Moreover, a distinct linear region (0.01–0.5 IU/mL) was observed with a limit of detection for 0.004 IU/mL, indicating the high sensitivity of ratiometric fluorescent probe.

In addition, ratiometric probe demonstrated excellent target specificity and anti-interference ability with nearly negligible signal fluctuation (<±5%) towards 18 representative interferents, including ions, thiols, proteins,

nucleases, and enzymatic species (Figure 3D,E) at concentrations equal to or higher than their physiological levels in human blood, indicating that the ratiometric signal primarily originated from enzymatic cleavage rather than nonspecific matrix interactions. Meanwhile, the time-dependent kinetic profile of ratiometric probe was evaluated to determine the response speed (Figure 3F). Due to the different catalytic kinetics of various DUB enzymes, distinct response dynamics were observed at low (0.1 IU/mL), medium (0.5 IU/mL), and high (1.0 IU/mL) activities, with higher activity levels producing faster signal evolution. Notably, plateau values were acquired within 30 min, inferring that the average response speed was determined to be 30 min, which was consistent with the previous reports [36].

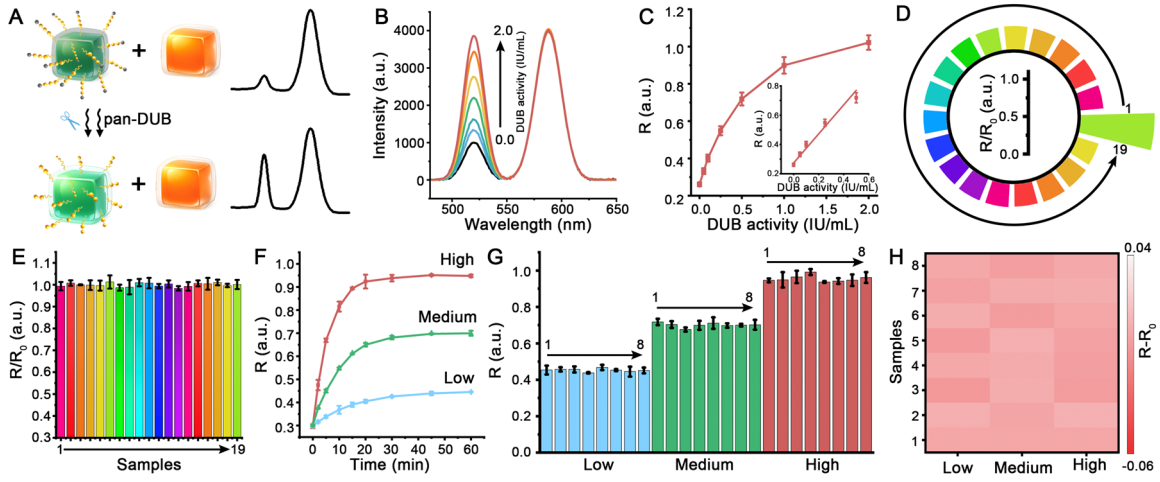

Figure 3. Response evaluation of the dual-emission ratiometric probe for pan-DUB activity sensing. (**A**) Schematic illustration of the probe response mechanism. (**B**) Fluorescence spectra of the dual-emission probe at increasing pan-DUB activities (0–2.0 IU/mL). (**C**) Calibration curve between $R = I_{green}/I_{orange}$ and pan-DUB activity. Inset: linear relationship between R and pan-DUB activity. (**D**) Selectivity of as-prepared ratiometric probe towards different interferences (1) ALP, (2) ascorbic_acid, (3) BSA, (4) Ca^{2+}, (5) Caspase-3, (6) Cl^{-}, (7) DNase, (8) GSH, (9) Glucose, (10) HAS, (11) K^{+}, (12) Lysozyme, (13) Mg^{2+}, (14) Na^{+}, (15) RNase, (16) Trypsin, (17) Urea, (18) Uric acid (19) pan-DUB enzyme mimics. (**E**) Anti-interference performance of as-prepared ratiometric probe towards (1) ALP, (2) ascorbic_acid, (3) BSA, (4) Ca^{2+}, (5) Caspase-3, (6) Cl^{-}, (7) DNase, (8) GSH, (9) Glucose, (10) HAS, (11) K^{+}, (12) Lysozyme, (13) Mg^{2+}, (14) Na^{+}, (15) RNase, (16) Trypsin, (17) Urea, (18) Uric acid (19) pan-DUB enzyme mimics. (**F**) Reaction kinetics of the probe at low (0.1 U/mL), medium (0.5 U/mL), and high activity levels (1.0 U/mL) within 60 min. (**G**) Fluorescent response of as-prepared ratiometric probe in different environment (1) PBS Buffer with pH = 7.4, (2) 10% FBS diluted with PBS (pH = 7.4), (3) 50% FBS diluted with PBS (pH = 7.4), (4) High salt buffer with 300 mM NaCl in PBS (pH = 7.4), (5) MES buffer with pH = 5.5, (6) Tris-HCl buffer with pH = 9.0 (7) Hemolyzed buffer (2–5 mg/mL hemoglobin), and lipemic matrices (200–500 mg/dL triglycerides) at low (0.1 U/mL), medium (0.5 U/mL), and high activity levels (1.0 U/mL). (**H**) Corresponding heatmap of $\Delta R = R - R_0$ for multiple biological mimicking matrices.

Importantly, PQD-based ratiometric probe exhibited excellent translational suitability and signal stability across different recognition environments. As shown in Figure 3G, the probe was challenged under eight biologically relevant conditions, including serum matrices, high-salt solutions, pH fluctuations, hemolysis, and lipemic interference. Across low/medium/high activity levels, the R value remained close to the buffer reference with an ultralow discrepancy of <5%, which was mainly due to the homologous lattice composition, unified surface chemistry, and matched dielectric environments under identical excitation of two perovskite nanocrystals, ensuring that environmental fluctuations impart near-identical perturbations to both channels. The ratio difference ΔR between the response R value in different buffer (R) and PBS buffer (R_0) showed a negligible variation (Figure 3H), confirming that the ratiometric strategy effectively suppressed the matrix-induced artifacts (serum dilution, ionic strength, pH variation, hemolysis, and lipid-rich matrices). Consenquently, PQD-based ratiometric probe achieved reliable readout across physiologically relevant environments, which has significant advantages over recent reported works (Table S1).

3.4. Correlation of Serum pan-DUB Activity with Cognitive Impairment in PND Mouse Model

To investigate the pathological relevance of pan-DUB activity regulation in PND, PND mouse model was first established and validated using Y-maze behavioral assays. As shown in Figure 4A, PND mice exhibited a significant reduction in spontaneous alternation rates compared with sham-operated controls, indicating impaired spatial working memory. In contrast, the total number of arm entries remained comparable between the two groups (Figure 4B), which effectively excluded the potential confounding effects arising from altered locomotor activity, confirming the successful establishment of a cognitive impairment phenotype characteristic of PND. Subsequently, serum pan-DUB activity was evaluated using the dual-emission ratiometric fluorescent probe. As shown in Figure 4C, the ratiometric signal R was significantly elevated in PND mice relative to sham controls, suggesting enhanced systemic deubiquitinating activity after surgery. Quantitatively, ratiometric readouts were converted into equivalent pan-DUB activity values using the calibration curve established in vitro. As shown in Figure 4D, PND mice displayed a marked increase in serum pan-DUB activity (IU/mL) compared with sham animals, further corroborating the upregulation of deubiquitinating enzymes in the PND state. Crucially, a strong inverse correlation between pan-DUB activity and cognitive performance within the PND cohort was revealed in Figure 4E, pan-DUB activity exhibited a robust negative correlation with Y-maze spontaneous alternation rates (Pearson $r = -0.94$, $p < 0.001$), indicating that elevated deubiquitinating activity is closely associated with the severity of working memory impairment. Finally, receiver operating characteristic (ROC) analysis was performed to assess the discriminative power of serum pan-DUB activity for distinguishing PND mice from sham controls. As shown in Figure 4F, pan-DUB activity achieved near-perfect classification performance, yielding an area under the curve (AUC) of 1.00 in this cohort with small sample size, which showed strong diagnostic potential of serum pan-DUB as a biomarker for PND using dual-emission ratiometric sensing strategy. For future clinical translation, large-scale, multi-center and diverse clinical sample validations are still required to further verify the diagnostic accuracy and reliability of serum pan-DUB activity as a biomarker for PND.

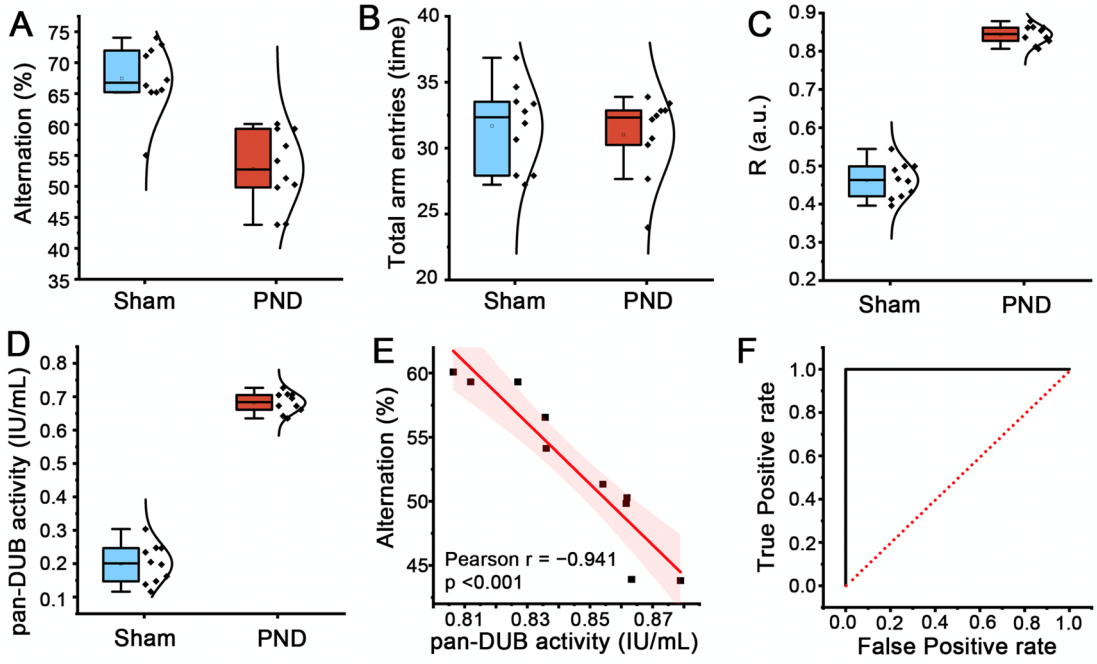

Figure 4. Serum pan-DUB activity is elevated in PND mice and tightly associated with cognitive impairment. (**A**) Y-maze spontaneous alternation rates of sham-operated and PND mice. (**B**) Total arm entries in the Y-maze, indicating comparable locomotor activity between sham and PND mice. (**C**) Ratiometric fluorescence response R of serum samples of sham and PND groups measured by the dual-emission probe. (**D**) Corresponding quantified serum pan-DUB activity in sham and PND groups. (**E**) Correlation analysis between serum pan-DUB activity and Y-maze spontaneous alternation rates in PND mice. (**F**) Receiver operating characteristic (ROC) analysis of serum pan-DUB activity for discriminating PND mice from sham controls. Data are presented as mean ± S.D. ($n = 32$ per group).

4. Conclusions

In conclusion, we developed a homogeneous dual-emission ratiometric fluorescent platform that enabled robust quantification of pan-DUB activity in highly heterogeneous biological fluids. By employing structurally

correlated $CsPbBr_3@SiO_2$ and $CsPbBr_{1.5}I_{1.5}@SiO_2$ PQDs as spectrally separated emitters, dual-emission ratiometric fluorescent platform achieved excellent uniform fluorescent responses towards the various pan-DUB activity under different measurement conditions across protein-rich, high-ionic-strength, and optically complex environments. Moreover, Conformal SiO_2 encapsulation endowed both emission channels with long-term aqueous stability, preserving more than 95% of ratiometric signals after prolonged storage for over 30 days and repeated irradiation for 15 times, respectively. In addition, the probe exhibited sensitive and reliable pan-DUB activity sensing ability with a wide dynamic range of 0.01–2 IU/mL with LOD for 0.004 IU/mL with high selectivity. Accordingly, by using as-prepared ratiometric fluorescent platform, it was found that serum pan-DUB activity was significantly elevated relative to sham-operated controls and showed a strong negative correlation with spatial working memory performance (Pearson $r = -0.94$) in a perioperative neurocognitive disorder mouse model, suggesting a systemic deubiquitination dysregulation to cognitive impairment. Complete separation between PND and control groups based on serum pan-DUB activity alone was successfully achieved with AUC = 1.00, reflecting its diagnostic potential for PND. This study represented the first demonstration of leveraging pan-enzymatic activity as a diagnostic readout for PND, offering a fundamentally potential and more sensitive route for disease identification, which was inherently extensible to other pathological conditions characterized by aberrant enzymatic networks, including neurodegenerative, inflammatory, and metabolic disorders [37–39]. Finally, the homogeneous and compositionally unified architecture based on PQDs provided a versatile platform for precision ratiometric sensing, offering improved analytical accuracy and robustness that can be broadly extended to other biomarker-based diagnostics across diverse disease contexts [40–42].

Supplementary Materials

The additional data and information can be downloaded at: https://media.sciltp.com/articles/others/2606020913579421/NENP-26020091-SM.pdf. References [43–47] are cited in the supplementary materials. The additional data and information included the experimental methods and supplementary figures.

Author Contributions

R.S. and S.H.: experimental operation, data analysis, and writing (original draft preparation); E.F.: project design, writing (reviewing and editing). All authors have read and agreed to the published version of the manuscript.

Funding

National Natural Science Foundation of China (22404125 to E.F.), Scientific Research Founds of Shanghai Fourth People's Hospital (SY-XKZT-2024-1005 and sykyqd08801 to E.F.), and Shanghai Sailing Program (24YF2733400 to E.F.).

Institutional Review Board Statement

The study was conducted according to the guidelines of the Declaration of Helsinki, and approved by the Tongji University Animal Ethics Committee (protocol code TJBH20824101 and 2024.03.04).

Informed Consent Statement

Not applicable.

Data Availability Statement

All data are available in the article and its Supplementary Information. Additional requests can be directed to the corresponding author.

Conflicts of Interest

The authors declare no conflict of interest.

Use of AI and AI-Assisted Technologies

No AI tools were utilized for this paper.

References

1. Subramaniyan, S.; Terrando, N. Neuroinflammation and Perioperative Neurocognitive Disorders. *Anesth. Analg.* **2019**, *128*, 781–788.
2. Eckenhoff, R.G.; Maze, M.; Xie, Z.; et al. Perioperative Neurocognitive Disorder: State of the Preclinical Science. *Anesthesiology* **2020**, *132*, 55–68.
3. Kong, H.; Xu, L.M.; Wang, D.X. Perioperative Neurocognitive Disorders: A Narrative Review Focusing on Diagnosis, Prevention, and Treatment. *CNS Neurosci. Ther.* **2022**, *28*, 1147–1167.
4. Jia, S.; Yang, H.; Huang, F.; et al. Systemic Inflammation, Neuroinflammation and Perioperative Neurocognitive Disorders. *Inflamm. Res.* **2023**, *72*, 1895–1907.
5. Li, R.; Zhang, Y.; Zhu, Q.X.; et al. The Role of Anesthesia in Peri-operative Neurocognitive Disorders: Molecular Mechanisms and Preventive Strategies. *Fundam. Res*. **2024**, *4*, 797–805.
6. Wang, Z.R.; Yang, W. Impaired Capacity to Restore Proteostasis in the Aged Brain after Ischemia: Implications for Translational Brain Ischemia Research. *Neurochem. Int.* **2019**, *127*, 87–93.
7. Zhang, L.L.; Xiao, F.; Zhang, J.; et al. Dexmedetomidine Mitigated NLRP3-Mediated Neuroinflammation via the Ubiquitin-Autophagy Pathway to Improve Perioperative Neurocognitive Disorder in Mice. *Front. Pharmacol*. **2021**, *12*, 646265.
8. Ndoja, A.; Reja, R.; Lee, S.H.; et al. Ubiquitin Ligase COP1 Suppresses Neuroinflammation by Degrading c/EBPβ in Microglia. *Cell* **2020**, *182*, 1156–1169.
9. Kandel, R.; Jung, J.; Neal, S. Proteotoxic Stress and the Ubiquitin Proteasome System. *Semin. Cell. Dev. Biol*. **2024**, *156*, 107–120.
10. Hassiepen, U.; Eidhoff, U.; Meder, G.; et al. A Sensitive Fluorescence Intensity Assay for Deubiquitinating Proteases Using Ubiquitin-rhodamine110-glycine as Substrate. *Anal. Biochem.* **2007**, *371*, 201–207.
11. Lee, J.; Kane, B.J.; Khanwalker, M.; et al. Development of an Electrochemical Impedance Spectroscopy Based Biosensor for Detection of Ubiquitin C-Terminal Hydrolase L1. *Biosens. Bioelectron*. **2022**, *208*, 114232.
12. Kummari, E.; Alugubelly, N.; Hsu, C.Y.; et al. Activity-Based Proteomic Profiling of Deubiquitinating Enzymes in *Salmonella*-Infected Macrophages Leads to Identification of Putative Function of UCH-L5 in Inflammasome Regulation. *PLoS ONE* **2015**, *10*, e0135531.
13. Kroll, M.H.; Elin, R.J. Interference with Clinical Laboratory Analyses. *Clin. Chem.* **1994**, *40*, 1996–2005.
14. Hawkins, C.L.; Davies, M.J. Detection, Identification, and Quantification of Oxidative Protein Modifications. *J. Biol. Chem*. **2019**, *294*, 19683–19708.
15. Wang, J.M.; Song, J.; Wang, X.Y.; et al. An ATMND/SGI Based Label-Free and Fluorescence Ratiometric Aptasensor for Rapid and Highly Sensitive Detection of Cocaine in Biofluids. *Talanta* **2016**, *161*, 437–442.
16. Dai, M.C.; Yang, Y.J.; Sarkar, S.; et al. Strategies to Convert Organic Fluorophores into Red/Near-Infrared Emitting Analogues and Their Utilization in Bioimaging Probes. *Chem. Soc. Rev*. **2023**, *52*, 6344–6358.
17. Mahbub, S.B.; Plöschner, M.; Gosnell, M.E.; et al. Statistically Strong Label-Free Quantitative Identification of Native Fluorophores in A Biological Sample. *Sci. Rep*. **2017**, *7*, 15792.
18. An, Q.; Xiang, S.R.; Zou, Y.Q. Recent Progresses in Combination Cancer Therapy Using Cyanine Dye-Based Nanoparticles. *Pharm. Sci. Adv.* **2024**, *2*, 100040.
19. Wang, W.X.; Gao, R.; Zhang, L.; et al. Fuel-Propelled Nanomotors for Acute Kidney Injury Applications. *Pharm. Sci. Adv.* **2024**, *2*, 100044.
20. Lin, Z.X.; Chen, Z.X.; Chen, Y.W.; et al. Hydrogenated Silicene Nanosheet Functionalized Scaffold Enables Immuno-Bone Remodeling. *Exploration* **2023**, *3*, 20220149.
21. Peng, Y.C.; Zhuang, Y.L.; Liu, Y.; et al. Bioinspired Gradient Scaffolds for Osteochondral Tissue Engineering. *Exploration* **2023**, *3*, 20210043.
22. Harati, J.; Wang, P.Y. Leveraging Integrative Technologies to Translate Stem Cell and Cell Reprogramming Potential for Neurodegenerative Diseases. *Eur. Cells Mater.* **2024**, *48*, 151–155.
23. Zhang, D.D.; Wang, P.Y. Intestinal Stem Cells (ISCs): ISCs-Derived Organoids for Disease Modeling and Therapy. *Eur. Cells Mater.* **2025**, *50*, 84–86.
24. Li, X.N.; Li, J.L.; Wang, W.X.; et al. Thermo-Oxidative Coupling Amplification Effect Unleashed by Tungsten-Based Polyoxometalate Nanoreactors Enables Synergistic Hyperthermia-Chemodynamic Therapy. *Part. Part. Syst. Charact.* **2026**, *43*, e00192.
25. Bai, Y.; Hao, M.; Ding, S.; et al. Surface Chemistry Engineering of Perovskite Quantum Dots: Strategies, Applications, and Perspectives. *Adv. Mater*. **2022**, *34*, 2105958.
26. Zhang, X.L.; Huang, H.H.; Zhao, C.Y.; et al. Surface Chemistry-Engineered Perovskite Quantum Dot Photovoltaics. *Chem. Soc. Rev*. **2025**, *54*, 3017–3060.

27. Feng, X.; Zhao, X.; Liu, J.; et al. Stable $CsPbBr_3$ Achieved by Porphyrin-Thiol Surface Management and Their Dual-Stimuli Responsive for Optical Encoding. *Adv. Mater. Interfaces* **2023**, *10*, 2201886.
28. Li, H.; Zhang, Y.; Wang, C.; et al. High-Purity Multicolor Electroluminescent Fibers by Incorporating with Light-Conversion Perovskite Quantum Dots. *Adv. Optical Materials* **2025**, *13*, 2403573.
29. Shamsi, J.; Urban, A.S.; Imran, M.; et al. Metal Halide Perovskite Nanocrystals: Synthesis, Post-Synthesis Modifications, and Their Optical Properties. *Chem. Rev*. **2019**, *119*, 3296–3348.
30. Huang, H.; Polavarapu, L.; Sichert, J.; et al. Colloidal Lead Halide Perovskite Nanocrystals: Synthesis, Optical Properties and Applications. *NPG Asia Mater.* **2016**, *8*, e328.
31. Kumar, P.; Patel, M.; Park, C.; et al. Highly Luminescent Biocompatible $CsPbBr_3@SiO_2$ Core-Shell Nanoprobes for Bioimaging and Drug Delivery. *J. Mater. Chem. B.* **2020**, *8*, 10337–10345.
32. Sun, C.; Zhang, Y.; Ruan, C.; et al. Efficient and Stable White LEDs with Silica-Coated Inorganic Perovskite Quantum Dots. *Adv. Mater.* **2016**, *28*, 10088–10094.
33. Tang, W.; Becker, M.L. "Click" Reactions: A Versatile Toolbox for the Synthesis of Peptide-Conjugates. *Chem. Soc. Rev.* **2014**, *43*, 7013–7039.
34. Song, W.; Wang, Y.; Wang, B.; et al. Super Stable $CsPbBr_3@SiO_2$ Tumor Imaging Reagent by Stress-Response Encapsulation. *Nano. Res.* **2020**, *13*, 795–801.
35. Kosovari, M.; Buffeteau, T.; Thomas, L.; et al. Silanization Strategies for Tailoring Peptide Functionalization on Silicon Surfaces: Implications for Enhancing Stem Cell Adhesion. *ACS Appl. Mater. Interfaces* **2024**, *16*, 29770–29782.
36. Li, Y.A.; Deng, B.; Chen, H.T.; et al. A Ratiometric Fluorescent Probe for the Detection of β-Galactosidase and Its Application. *RSC Adv.* **2021**, *11*, 13341–13347.
37. Feng, H.R.; Liu, Y.; Wang, X.; et al. Cerebrospinal Fluid Biomarkers of Neuroinflammation and Postoperative Neurocognitive Disorders in Patients Undergoing Orthopedic Surgery: A Systematic Review and Meta-Analysis. *Int. J. Surg.* **2025**, *111*, 3573–3588.
38. Sakamoto, S.; Hiraide, H.; Minoda, M.; et al. Identification of Activity-Based Biomarkers for Early-Stage Pancreatic Tumors in Blood Using Single-Molecule Enzyme Activity Screening. *Cell Rep. Methods* **2024**, *4*, 100688.
39. Pathan, S.U.; Kharwar, A.; Ibrahim, M.A.; et al. Enzymes as Indispensable Markers in Disease Diagnosis. *Bioanalysis* **2024**, *16*, 485–497.
40. Wang, X.; Ding, Q.; Groleau, R.R.; et al. Fluorescent Probes for Disease Diagnosis. *Chem. Rev.* **2024**, *124*, 7106–7164.
41. Michalet, X.; Pinaud, F.F.; Bentolila, L.A.; et al. Quantum Dots for Live Cells, in Vivo Imaging, and Diagnostics. *Science* **2005**, *307*, 538–544.
42. Wang, S.Z.; Yousefi Amin, A.A.; Wu, L.Z.; et al. Perovskite Nanocrystals: Synthesis, Stability, and Optoelectronic Applications. *Small Struct*. **2021**, *2*, 2000124.
43. Dang, L.C.; Melandri, F.D.; Stein, R.L. Kinetic and Mechanistic Studies on the Hydrolysis of Ubiquitin C-Terminal 7-Amido-4-Methylcoumarin by Deubiquitinating Enzymes. *Biochemistry* **1998**, *37*, 1868–1879.
44. Geurink, P.P.; Van Tol, B.D.M.; Van Dalen, D.; et al. Development of Diubiquitin-Based FRET Probes to Quantify Ubiquitin Linkage Specificity of Deubiquitinating Enzymes. *ChemBioChem* **2016**, *17*, 816–820.
45. Gutkin, S.; Gandhesiri, S.; Brik, A.; et al. Synthesis and Evaluation of Ubiquitin-Dioxetane Conjugate as a Chemiluminescent Probe for Monitoring Deubiquitinase Activity. *Bioconjugate Chem.* **2021**, *32*, 2141–2147.
46. Shorkey, S.A.; Du, J.; Pham, R.; et al. Real-Time and Label-Free Measurement of Deubiquitinase Activity with a MspA Nanopore. *ChemBioChem* **2021**, *22*, 2688–2692.
47. Conole, D.; Cao, F.; Am Ende, C.W. Discovery of a Potent Deubiquitinase (DUB) Small-Molecule Activity-Based Probe Enables Broad Spectrum DUB Activity Profiling in Living Cells. *Angew. Chem. Int. Ed.* **2023**, *62*, e202311190.